Crystal growth and magnetic properties of LaMn$_{0.91}$Sb$_2$ and NdMn$_{0.88}$Sb$_2$

Yong Li (李勇),[1,2,3,*] Meng Yang (杨萌) ⓘ,[1,*] Dayu Yan (闫大禹),[1] Shanshan Miao (苗杉杉),[1] Huaixin Yang (杨槐馨),[1,3,†]
Hai L. Feng (冯海) ⓘ,[1,4,‡] and Youguo Shi (石友国)[1,2,4,§]

[1]*Beijing National Laboratory for Condensed Matter Physics and Institute of Physics, Chinese Academy of Sciences, Beijing 100190, China*
[2]*Center of Materials Science and Optoelectronics Engineering, University of Chinese Academy of Sciences, Beijing 100190, China*
[3]*School of Physical Sciences, University of Chinese Academy of Sciences, Beijing 100190, China*
[4]*Songshan Lake Materials Laboratory, Dongguan, Guangdong 523808, China*

In this work, single crystals of LaMn$_{0.91}$Sb$_2$ and NdMn$_{0.88}$Sb$_2$ with deficiencies of Mn have been successively grown by using the Bi-flux method. They all crystallize in the HfCuSi$_2$-type tetragonal structure with space group $P4/nmm$ (No.129). LaMn$_{0.91}$Sb$_2$ displays signs of successive antiferromagnetic transitions around 133 and 108 K for $H||c$. In the case of $H\perp c$, LaMn$_{0.91}$Sb$_2$ shows signs of weak ferromagnetic transition around 138 K and antiferromagnetic transition at 56 K. However, there is no anomaly observed in the temperature-dependent specific heat curve. For NdMn$_{0.88}$Sb$_2$ measured with $H||c$, the Mn sublattice orders antiferromagnetically below 170 K and the Nd sublattice shows successive antiferromagnetic orders at 34 and 26 K. The antiferromagnetic state of Nd sublattice can be induced to be a ferromagnetic state through a spin-flop transition at 2 K. When $H\perp c$, the Mn sublattice displays antiferromagnetic orders at 171, 156, and 74 K. The Nd sublattice orders antiferromagnetically below 32 K. Ferromagnetic state for the Nd sublattice is induced by magnetic fields through a spin-flop transition at 2 K. Magnetic phase diagrams for NdMn$_{0.88}$Sb$_2$ are depicted for cases of $H||c$ and $H\perp c$, respectively. LaMn$_{0.91}$Sb$_2$ and NdMn$_{0.88}$Sb$_2$ show metallic behavior. Negative magnetoresistance in LaMn$_{0.91}$Sb$_2$ and NdMn$_{0.88}$Sb$_2$ are possibly related to canted-antiferromagnetic orders of Mn sublattices.

I. INTRODUCTION

Ternary compounds with a general formula $AMPn_2$ (A = a rare earth or alkali earth element; M = transition metal; Pn = Sb, or Bi), usually crystalize in tetragonal structures ($P4/nmm$ or $I4/mmm$) or orthorhombic structures ($Pnma$ or $Imm2$) with A ions sandwiched between two-dimensional pnictides layer and the layer of edge-sharing $MPn_{4/4}$ tetrahedra [1–17]. In recent years, compounds with M = Mn have attracted great attention due to their exceptional electronic bands, such as quasi-two-dimensional massless Dirac fermions in CaMnSb$_2$ and SrMnSb$_2$ [2,8,18,19], chiral surface state, and profound Shubnikov–de Haas oscillations in a noncentrosymmetric Dirac semimetal BaMnSb$_2$ [20], quantum Hall effect in bulk antiferromagnet EuMnBi$_2$ [21], as well as large negative magnetoresistance in EuMnSb$_2$ [22,23].

When A is divalent alkali earth or Yb^{2+} ion, $AMnPn_2$ (Pn = Sb or Bi) generally displays antiferromagnetic (AFM) orders of Mn ions near room temperature [24–26]. Studies on YbMnSb$_2$ indicate that different magnetic structures can affect the topological nature of fermions [27]. When A is a trivalent rare earth element, the $AMnPn_2$ (Pn = Sb or Bi) compounds commonly have deficiencies on Mn sites

[16,17,28], and their magnetic properties are getting richer because of the interactions between magnetic active rare-earth ions and Mn ions. For example, PrMn$_{1-x}$Sb$_2$ shows two AFM transitions related to Pr and Mn moments, respectively, and has a complex magnetic phase diagram [28]. A recent study on EuMnSb$_2$ indicates that the magnetic sublattice of rare-earth ions has an influence on the conduction electrons near the Dirac point [29]. Polycrystalline samples of LaMnSb$_2$ and NdMnSb$_2$ with weak ferromagnetic (FM) orders of the Mn sublattice at ∼ 310 and ∼ 250 K, respectively, have been reported, and second magnetic order at ∼ 45 K associated with Nd sublattice was suggested for NdMnSb$_2$ [17]. In this work, single crystals of LaMnSb$_2$ and NdMnSb$_2$ are successfully grown, and their detailed magnetic properties and electrical resistivity are reported.

II. EXPERIMENT

Single crystals of NdMnSb$_2$ and LaMnSb$_2$ were grown by using Bi-flux. High purity elements Nd (ingot, 99.9%, Purui Advanced Material Technology Co. Ltd., Beijing, China), La (ingot, 99.9%, Purui Advanced Material Technology Co. Ltd., Beijing, China), Mn (pieces, 999.98%, Alfa Aesar), Sb (pills, 99.999%, Alfa Aesar), and Bi (pills, 99.999%, Alfa Aesar) were used. Start materials with a molar ratio of Nd/La : Mn : Sb : Bi = 1 : 1 : 2 : 10 were weighed and placed in alumina crucibles. The crucibles were then sealed in evacuated quartz tubes under a high vacuum. The sealed tubes were heated up to 1050 °C over 10 h and then dwelt for 24 h, before slowly

———————
*These authors contributed equally.
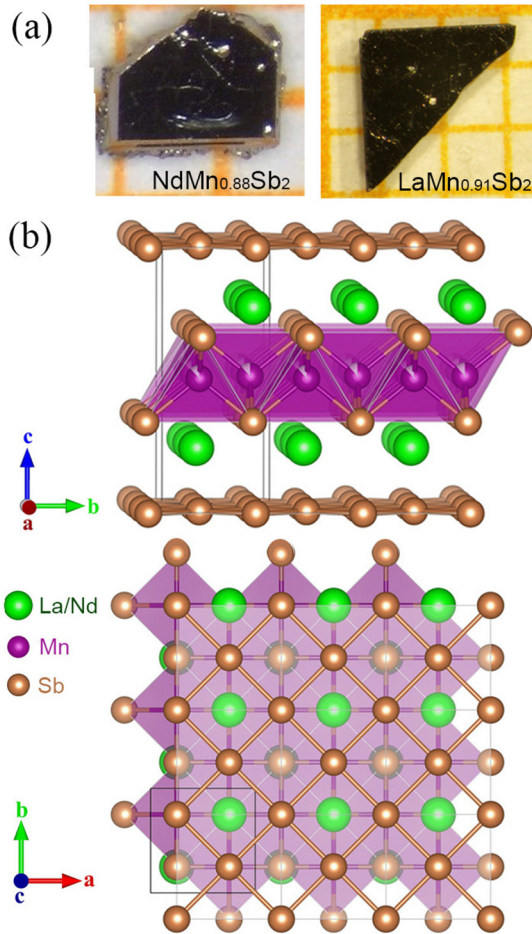†Corresponding authors: hxyang@iphy.ac.cn
‡hai.feng@iphy.ac.cn
§ygshi@iphy.ac.cn

FIG. 1. (a) Images of typical single crystals for $LaMn_{0.91}Sb_2$ and $NdMn_{0.88}Sb_2$. (b) Crystal structures for $AMn_{1-x}Sb_2$ (A = La or Nd) view along with a- and c-axis.

cooling to 650 °C at a rate of 2 °C/h. The Bi-flux was removed by centrifuging. Plate-like crystals with a typical size of 5 × 5 × 1 mm³ were obtained [see Fig. 1(a)]. The crystals were stable in the air.

Single-crystal x-ray diffraction data were collected on a Bruker D8 VENTURE PHOTO II diffractometer with Mo Kα ($\lambda = 0.71073$ Å) radiation. Unit cell refinement and data merging were done with the SAINT program, and an absorption correction was applied using multi-Scan. Structural solutions were obtained by intrinsic phasing methods using the program APEX3 [30], and the final refinement was completed by a full-matrix least-squares method on F^2 using the SHELXL-2016/6 programs [31,32]. Powder x-ray diffraction (PXRD) was performed in Rigaku SmartLab 9kW (Cu Kα) and structure refinement was performed with the program package GSAS-II [33]. Elemental analysis of the samples was performed using energy dispersive x-ray spectroscopy (EDX) in a Hitachi S-4800 scanning electron microscopy at an accelerating voltage of 15 kV.

Plate-like crystals were used for magnetic and specific heat capacity (C_p) measurements. The magnetic properties were measured in a Magnetic Properties Measurement System (MPMS-III, Quantum Design Inc.). Magnetic susceptibility was measured at temperatures between 2 and 300 K under varied magnetic fields (H) with field-cooling (FC) and zero-field-cooling (ZFC) conditions. Isothermal magnetizations were measured between magnetic fields of -70 kOe to 70 kOe. The C_p was measured by a thermal-relaxation method from 2 to 300 K in a Physical Property Measurement System (PPMS-9T, Quantum Design Inc.). The samples were thermally connected to the holder stage with Apiezon N grease. Electrical resistivity (ρ) and magnetoresistance were measured in the PPMS-9T with the standard four-probe method.

III. RESULTS AND DISCUSSIONS

Analysis of single-crystal x-ray diffraction data for $NdMnSb_2$ and $LaMnSb_2$ indicated that they crystallize in the HfCuSi$_2$-type tetragonal structure with space group $P4/nmm$ (No.129) which is consistent with the previous polycrystalline studies [17]. The refined cell parameters are a = 4.320(1) Å and c = 10.670(1) Å for $NdMnSb_2$ and a = 4.384(3) Å, and c = 10.839(2) Å for $LaMnSb_2$. $LaMnSb_2$ has a relatively larger unit cell than $NdMnSb_2$ due to the larger ionic radius of La^{3+} than Nd^{3+}. The structure refinements indicate a considerable amount of Mn deficiency in both compounds, and the refined compositions are $LaMn_{0.91}Sb_2$ and $NdMn_{0.88}Sb_2$. The goodness of fit values for the refinements are 1.227 and 1.208 for $LaMn_{0.91}Sb_2$ and $NdMn_{0.88}Sb_2$, respectively. Detailed crystallographic information, refined atomic positions, and displacement parameters for $LaMn_{0.91}Sb_2$ and $NdMn_{0.88}Sb_2$ are listed in Tables S1, S2, and S3 in the Supplemental Material (SM) [34]. It should be noted that deficiencies of Mn sites have been reported in most AMnSb$_2$ compounds with a trivalent rare-earth ion in the A site. When A is a divalent ion, $CaMnSb_2$, $BaMnSb_2$, and $YbMnSb_2$ are stochiometric [18,20,27]. Their electron-partition can be simplified as $A^{2+}Mn^{2+}Sb^{3-}Sb^{1-}$ by using the Zintl concept when A is a divalent ion. Thus, it becomes electron-rich when A is a trivalent ion and this oversimplified scenario can somehow explain the tendency for deficiencies of Mn sites [24]. The Mn deficiencies were also reported for the polycrystalline samples with compositions of $LaMn_{0.87}Sb_2$ and $NdMn_{0.83}Sb_2$ [17]. The crystal structures for $LaMn_{0.91}Sb_2$ and $NdMn_{0.88}Sb_2$ are illustrated in Fig. 1(b). Their structures consist of layers of edge-sharing MnSb$_{4/4}$ tetrahedra, two-dimensional square nets formed by Sb atoms, and Nd or La cations between them. The bond lengths of Mn-Sb1 are 2.7776(7) Å for $NdMn_{0.88}Sb_2$ and 2.7726(7) Å for $LaMn_{0.91}Sb_2$, which are comparable to 2.7643(7) Å reported for $YbMnSb_2$.

The chemical compositions of the as-prepared single crystals were further examined using EDX. The EDX data, measured at several points, are shown in the SM (See Tables S4 and S5) [34]. There are Bi elements in both $LaMn_{0.91}Sb_2$ and $NdMn_{0.88}Sb_2$ single crystals. The normalized elements ratio for $LaMn_{0.91}Sb_2$ is La : Mn : Sb : Bi = 1 : 0.92 : 1.97 : 0.12, and for $NdMn_{0.88}Sb_2$ is Nd : Mn : Sb : Bi = 1 : 0.86 : 1.99 : 0.09. The ratio between La(Nd): Mn is close to the composition refined from the single-crystal x-ray diffraction data. Single crystals of $LaMn_{0.91}Sb_2$ and $NdMn_{0.88}Sb_2$ were ground to be powders and their powder x-ray diffraction patterns were collected at room temperature for both compounds.
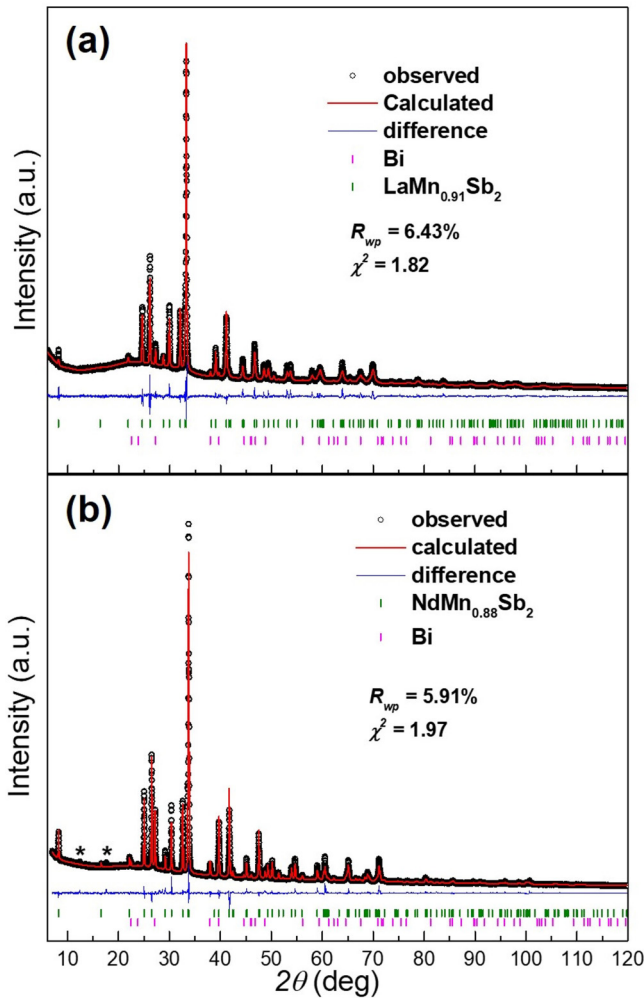
FIG. 2. Room-temperature powder x-ray diffraction patterns for powdered single crystals of (a) $LaMn_{0.91}Sb_2$ and (b) $NdMn_{0.88}Sb_2$. Two unidentified impurity peaks are marked with asterisks in the $NdMn_{0.88}Sb_2$ sample.

The x-ray diffraction patterns, shown in Fig. 2, affirm the presence of flux Bi in both compounds.

Magnetism. Temperature-dependent magnetizations, $M(T)$, of $LaMn_{0.91}Sb_2$ measured under varied H ($H||c$) are shown in Fig. 3(a). The $M(T)$ curves of $LaMn_{0.91}Sb_2$ measured under 0.1 and 1 kOe show peaks around 133 and 108 K [see the inset in Fig. 3(a)], indicating successive AFM transitions in $LaMn_{0.91}Sb_2$. The peak around 108 K becomes less prominent with increasing of H to 10 kOe and disappears in the 30 kOe curve [see Fig. 3(a)]. The peaks around 133 K (defined as $T_{N||}$) survive up to 30 kOe, and the $M(T)$ curves measured under 50 and 70 kOe show a monotonic increase with cooling and display a slope change around $T_{N||}$ (see corresponding dM/dT curves in Fig. S1 in the SM [34]). For $H\perp c$, $M(T)$ curves of $LaMn_{0.91}Sb_2$ measured under varied H are shown in Fig. 3(b). The curves measured with 0.1 and 1 kOe display peaks around 56 K, suggesting an AFM order. Above this transition, the $M(T)$ curves show a slope change around 138 K, defined as $T_{N\perp}$ (see the corresponding dM/dT curve shown in Fig. S2 in the SM [34]). M increases faster below $T_{N\perp}$, indicating a weak

FM transition. Weak FM order at ~ 310 K was previously reported for the polycrystalline samples of $LaMnSb_2$ [17]. The peak around 56 K is suppressed when the $M(T)$ curves measured under 10 kOe and above [see Fig. 3(b)], and $M(T)$ curves measured under 10, 30, 50, and 70 kOe all show slope changes around $T_{N\perp}$ (see corresponding dM/dT curves shown in Fig. S3 in the SM [34]). It should be noted that the ZFC and FC curves measured under 0.1 kOe show divergence below ~ 250 K for both $H||c$ and $H\perp c$ and this divergence is suppressed when H is 1 kOe or larger, indicating a small ferromagnetic component in this sample.

Isothermal magnetizations, $M(H)$, for $LaMn_{0.91}Sb_2$ measured with $H||c$ at different temperatures, are shown in Fig. 3(c). The $M(H)$ curves measured at 300 and 400 K (above $T_{N||}$) deviate from linearity around the zero magnetic field region and can be regarded as a straight line superposed with a small FM component (see Fig. S4 in the SM [34]). This weak FM component saturates with saturated magnetizations (M_s) of 0.047 μ_B/f.u. and 0.029 μ_B/f.u. at 300 and 400 K, respectively. It can not exclude the possibility that this small FM component is intrinsic. But it is more likely due to impurity phases. A study on $PrMnSb_2$ found a similar superposition of small FM components in the $M(H)$ curves measured at 400 and 250 K [9], and one possible impurity is MnSb with an FM transition at ~ 590 K [35]. Though there is no clear evidence of MnSb phase in the XRD pattern of $LaMn_{0.91}Sb_2$, the presence of a small amount (less than 1% wt) of MnSb cannot be excluded. The $M(H)$ curve measured at 100 K (below $T_{N||}$) shows linear behavior below 30 kOe, consistent with the AFM order, and displays a sharp increase around 30 kOe, indicating a field-induced metamagnetic transition. At 50 and 2 K, the $M(H)$ curves show sharp slope changes around 17 kOe and 30 kOe (critical fields defined from dM/dH curves shown in Fig. S5 in the SM [34]), indicating successive field-induced metamagnetic transitions of Mn sublattice. M tends to saturate when H is larger than 40 kOe and is about 1.1 μ_B/f.u. at 2 K and 70 kOe, which is much smaller than the M_s expected for a real FM state, thus indicating a field-induced weak FM state of Mn sublattice. For $H\perp c$, $M(H)$ curves of $LaMn_{0.91}Sb_2$ measured at 300, 100, and 2 K are shown in Fig. 3(d). The $M(H)$ curve measured at 300 K (above $T_{N\perp}$) is similar to the one measured with $H||c$, which can be regarded as a straight line superposed with a small FM component with a M_s of 0.40 μ_B/f.u. (see Fig. S6 in the SM [34]). The $M(H)$ curves measured at 2 and 100 K (below $T_{N\perp}$) show nonlinear behaviors and are consistent with the weak FM transition around $T_{N\perp}$. There is no indication of field-induced metamagnetic transition in the case of $H\perp c$. The M(H) curve measured at 2 K tends to saturate when H is larger than 30 kOe, and M is about 1.1 μ_B/f.u. at 2 K and 70 kOe.

Signs of successive AFM transitions are observed at 133 and 108 K for $LaMn_{0.91}Sb_2$ with $H||c$. In the case of $H\perp c$, the $M(T)$ curves show weak FM transition at 138 K and AFM transition at 56 K. In comparison with similar compounds $EuMnSb_2$ [29] and $PrMnSb_2$ [9,28] all having AFM orders for the Mn sublattices, AFM orders are expected for the Mn sublattice in $LaMn_{0.91}Sb_2$. The weak FM transition at 138 K may be a canted-AFM order. To further study these magnetic orders of $LaMn_{0.91}Sb_2$, temperature-dependent specific heat, $C_p(T)$, of $LaMn_{0.91}Sb_2$ was measured from 300 to 2 K
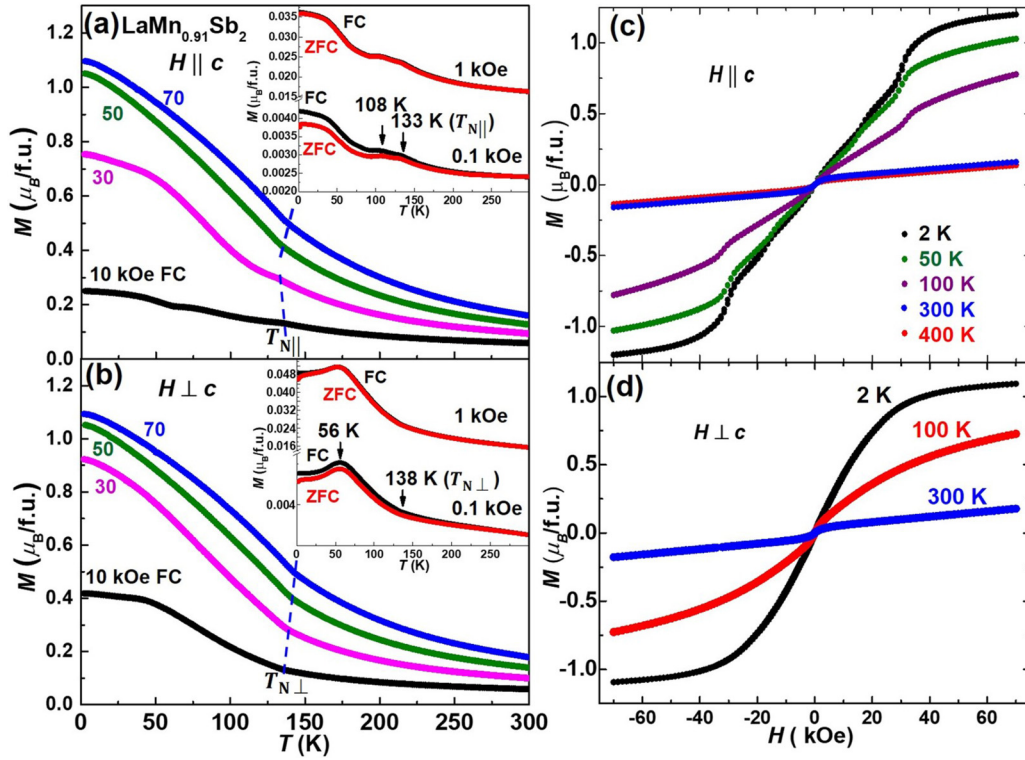
FIG. 3. (a) and (b) Temperature-dependent magnetizations of $LaMn_{0.91}Sb_2$ measured with $H||c$ and $H\perp c$, respectively. (c) and (d) Isothermal magnetizations of $LaMn_{0.91}Sb_2$ measured with $H||c$ and $H\perp c$, respectively.

(see Fig. 4). There is no clear anomaly around temperatures 138, 133, 108, and 56 K in the $C_p(T)$ curve of $LaMn_{0.91}Sb_2$. A possible explanation for the absence of anomaly in the $C_p(T)$ curve is that the magnetic entropy is distributed over a wide temperature range as evidenced by the signs of magnetic orders for $LaMn_{0.91}Sb_2$ observed at temperatures 138, 133, 108, and 56 K. Future measurements, such as neutron diffractions, are needed to study the successive magnetic orders in $LaMn_{0.91}Sb_2$.

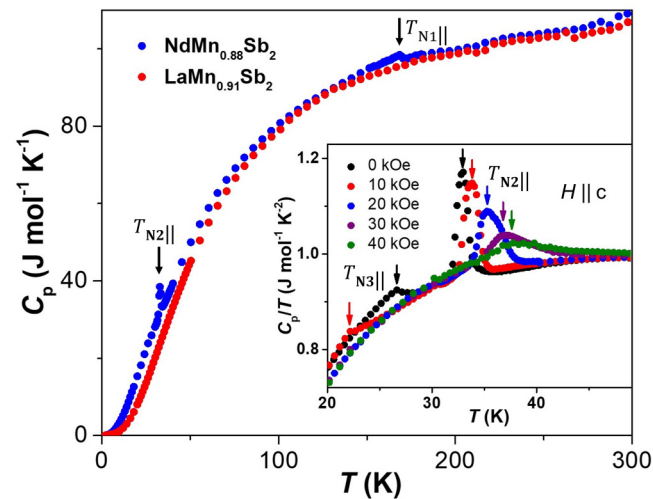FIG. 4. Temperature-dependent specific heat for $NdMn_{0.88}Sb_2$ and $LaMn_{0.91}Sb_2$. Inset shows the C_p/T vs. T data for $NdMn_{0.88}Sb_2$ measured between 20–50 K under varied H ($H||c$).

The $M(H)$ curves of $LaMn_{0.91}Sb_2$ measured at 2 K show field-induced metamagnetic transitions when $H||c$, but display a continuous increase of M with increasing of H when $H\perp c$. This suggests that the direction of magnetic moments of Mn is possibly parallel to the c axis (perpendicular to the two-dimensional layers) because that field-induced metamagnetic transitions generally occur when the applied H is parallel to the magnetic moments in a weak anisotropic system. This is consistent with neutron diffraction studies on $YbMnBi_2$ [36,37], $YbMnSb_2$ [27], $PrMnSb_2$ [9], and $EuMnSb_2$ [29,38] in which moments of Mn are mainly aligned parallel to the c axis (or perpendicular to the two-dimensional layers). The possibility of a small canting angle was suggested in $PrMnSb_2$ [9] and the study on $YbMnBi_2$ puts an upper limit of 3° on any canting of the ordered moment of Mn from the c-axis [37].

$M(T)$ curves of $NdMn_{0.88}Sb_2$ measured under 10, 20, 30, 50, and 70 kOe ($H||c$) are shown in Fig. 5(a). The $M(T)$ curve of $NdMn_{0.88}Sb_2$ measured under 10 kOe shows three features: a peak at 170 K, a kink around 34 K, and another peak at 26 K. The peak at 170 K (defined as $T_{N1||}$) indicates an AFM order. The magnetic order at $T_{N1||}$ is possibly due to an AFM order of Mn sublattice in $NdMn_{0.88}Sb_2$. The $T_{N1||}$ is comparable to the AFM order temperature of $\sim$175 K for Mn sublattice in $PrMnSb_2$ [9,28]. The long-range magnetic order at $T_{N1||}$ is also confirmed from the $C_p(T)$ data of $NdMn_{0.88}Sb_2$, showing a λ-type anomaly around 169 K (see Fig. 4). The $C_p(T)$ data of $NdMn_{0.88}Sb_2$ also shows a large anomaly around 34 K which is corresponding to the kink around 34 K (defined as $T_{N2||}$) in the $M(T)$ curve. The magnetic transition at $T_{N2||}$ is possibly due to a magnetic order of Nd sublattice. Below $T_{N2||}$, the magnetizations increase with further cooling, indicating that
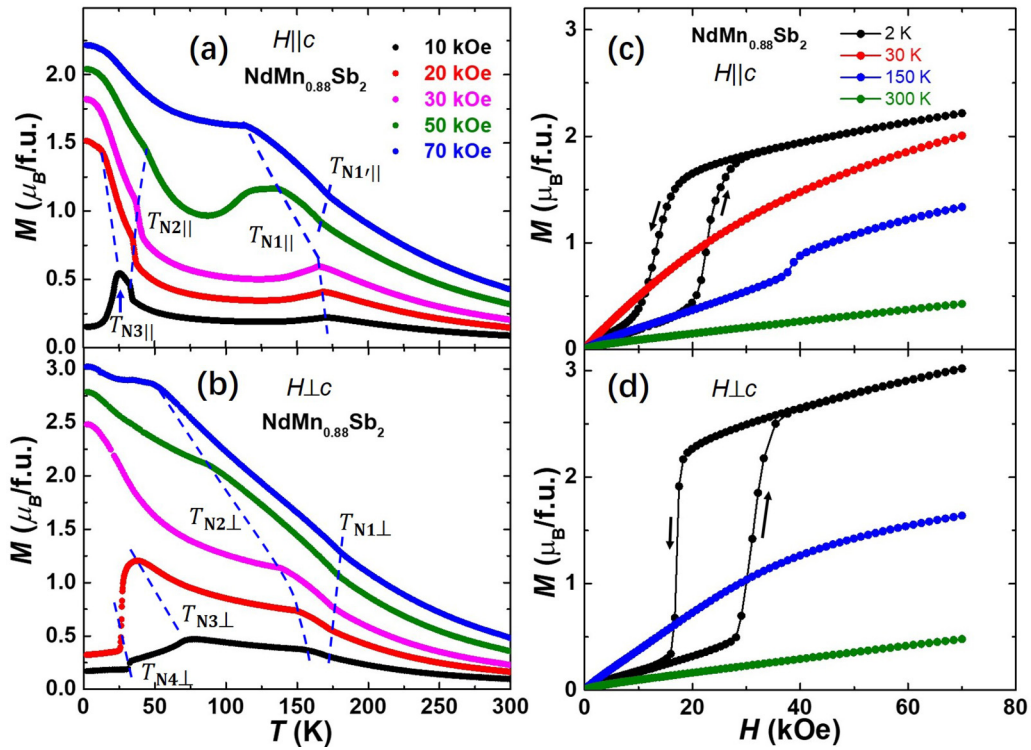
FIG. 5. (a) and (b) Temperature-dependent magnetizations of and NdMn$_{0.88}$Sb$_2$ measured with $H||c$ and $H\perp c$, respectively. (c) and (d) Isothermal magnetizations of and NdMn$_{0.88}$Sb$_2$ measured with $H||c$ and $H\perp c$, respectively.

the AFM order of Nd ions is possibly canted. With further cooling, the $M(T)$ curve shows another peak at 26 K (defined as $T_{N3||}$), which is possibly due to a reorientation of Nd moments from canting to collinear.

With increasing of H to 20 kOe and above, the AFM order of Nd at $T_{N3||}$ is almost suppressed, and the canted-AFM order of Nd at $T_{N2||}$ shifts toward higher temperatures and is suppressed at 70 kOe, indicating a possible field-induced FM state for Nd sublattice of NdMn$_{0.88}$Sb$_2$. This field-dependent behavior is also confirmed from field-dependent $C_p(T)$ data as shown in the inset of Fig. 4: anomalies corresponding to $T_{N3||}$ shift toward lower temperatures while anomalies corresponding to $T_{N2||}$ move toward higher temperatures with increasing of H. It should be noted that the single crystal was pulled away from the sample puck for the C_p measurement when $H = 50$ kOe was applied. The AFM order of Mn sublattice at $T_{N1||}$ is robust against H up to 30 kOe. With further increases of H to 50 and 70 kOe, the $T_{N1||}$ peaks are suppressed toward much lower temperatures. Kinks around 168 and 175 K (see corresponding dM/dT curves in Fig. S7 in the SM [34]), defined as $T_{N1'||}$, appear for $M(T)$ curves measured under 50 and 70 kOe, indicating that the Mn sublattice first undergoes a canted-AFM order before reaching the AFM order.

To further understand these magnetic transitions, $M(H)$ curves of NdMn$_{0.88}$Sb$_2$ measured with $H||c$ at different temperatures are shown in Fig. 5(c). The curve measured at 300 K shows linear behavior as expected for the paramagnetic state. The curve measured at 150 K (below $T_{N1||}$) shows a linear behavior with H up to 40 kOe, then shows a rapid increase of M, indicating a field-induced spin-flop transition

of Mn sublattice. This is consistent with the scenario proposed in the $M(T)$ parts that the Mn AFM state is robust up to 30 kOe and the Mn sublattice first undergoes a canted-AFM state before reaching the AFM state when measured at 50 and 70 kOe. The $M(H)$ curve measured at 30 K (between $T_{N2||}$ and $T_{N3||}$) shows nonlinear behavior, consistent with a canted-AFM state of Nd sublattice. At 2 K, the $M(H)$ curve shows linear behavior when H is not larger than 17 kOe, consistent with the AFM state. Above 17 kOe, the magnetizations increase rapidly with increasing magnetic fields, indicating a field-induced spin-flop transition. This spin-flop transition is possible first-order because a large magnetic hysteresis is observed. The critical field for increasing H ($H_{1||}$), is 22.5 kOe and the critical field for decreasing H ($H_{2||}$) is 13.0 kOe determined from the dM/dT curve (see Fig. S8 in the SM [34]). The spin-flop transition field for $H||c$ ($H_{SF||}$) is about 17.1 kOe according to the equation $H_{SF} = (H_1 H_2)^{1/2}$ [39]. When H is larger than ~50 kOe, M shows a linear correlation with H. Subtracting the linear component, the M_s of the resulting saturated FM component is 1.63 μ_B/f.u. (see Fig. S9 in the SM [34]). This value is close to an ordered moment of 1.69 μ_B for Nd^{3+} in a similar compound NdNiSb$_2$ having the same $P4/nmm$ space group as NdMn$_{0.88}$Sb$_2$ [40]. The Nd ions have comparable coordination of eight Sb ions in both compounds. These moments are lower than the theoretical moment of $g_J J = 3.27$ μ_B for a free Nd^{3+} ion ($J = 9/2$ and $g_J = 8/11$), indicating the electronic state of Nd ions is affected by the crystalline electric field.

$M(T)$ curves of NdMn$_{0.88}$Sb$_2$ measured under 10, 20, 30, 50, and 70 kOe ($H\perp c$) are shown in Figs. 5(b). Different from the 10 kOe $M(T)$ curve measured with $H||c$, the 10 kOe

curve measured with $H \perp c$ does not show a typical AFM peak around 170 K, but displays kinks at 171 and 156 K, and a peak around 74 K. The kink at 171 K (defined as $T_{N1\perp}$) indicates a canted-AFM transition of Mn sublattice. The Mn sublattice then undergoes a spin-reorientation at 156 K (defined as $T_{N2\perp}$) before reaching an AFM order at 74 K ($T_{N3\perp}$). At 32 K (defined as $T_{N4\perp}$), the 10 kOe M(T) curve shows a sharp drop, which should indicate an AFM order of Nd sublattice. The $T_{N4\perp}$ is close to the $T_{N2\|}$ (34 K) for the canted-AFM order of Nd sublattice when measured with $H\|c$. The $T_{N3\perp}$ and $T_{N4\perp}$ are suppressed toward lower temperatures when measured under 20 kOe, and disappear when H is 30 kOe or larger, indicating a field-induced magnetic-state change for both Mn sublattice and Nd sublattice. The transition at $T_{N1\perp}$ is robust against the increase of H, but $T_{N2\perp}$ shifts toward lower temperatures with the increase of H.

$M(H)$ curves of NdMn$_{0.88}$Sb$_2$ measured with $H \perp c$ at different temperatures are shown in Fig. 5(d). The $M(H)$ curve measured at 300 K shows linear behavior which is consistent with the paramagnetic state. At 150 K, the $M(H)$ curve is nonlinear which is consistent with the proposed canted-AFM state of Mn sublattice. At 2 K, the $M(H)$ curve shows linear behavior with H up to 27 kOe, which supports the proposed AFM ground state for both Mn and Nd sublattices. Above 27 kOe, the $M(H)$ curve deviates from linearity and shows a rapid increase, indicating a spin-flop transition. This spin-flop transition is also associated with large magnetic hysteresis. The critical fields are $H_{1\perp} = 31.4$ kOe for increasing H and $H_{2\perp} = 17.0$ kOe for decreasing H determined from the corresponding dM/dH curve (see Fig. S10 in the SM [34]). The spin-flop transition field for $H \perp c$, $H_{SF\perp}$, is about 23.1 kOe according to the equation $H_{SF} = (H_1 H_2)^{1/2}$ [39]. When H is larger than 40 kOe, the $M(H)$ curve shows a roughly linear behavior. Subtracting the linear component, the resulting $M(H)$ curve saturates above 50 kOe, and the M_S for the FM component is 2.2 μ_B/f.u. (see Fig. S11 in the SM [34]). This value is larger than the M_S observed for $H\|c$ (1.63 μ_B/f.u.) and suggests some FM contributions are from Mn sublattice due to the canted-AFM structure when H is 30 kOe or larger.

Magnetic phase diagrams of NdMn$_{0.88}$Sb$_2$ according to the $M(T)$, $M(H)$, and $C_p(T)$ data for both $H\|c$ and $H \perp c$ cases are shown in Figs. 6(a) and 6(b), respectively. In the case of $H\|c$, the Mn sublattice displays an AFM order below $T_{N1\|}$ when H is no more than 30 kOe. When H is larger than 30 kOe, the Mn sublattice first undergoes a canted-AFM state before reaching the AFM state. The Nd sublattice first undergoes a canted-AFM state below $T_{N2\|}$ before reaching the AFM state, and there is a field-induced FM state for Nd sublattice at low temperatures with $H_{SF\|} = 17.1$ kOe at 2 K. For $H \perp c$, the Mn sublattice undergoes a canted-AFM-1 state and a canted-AFM-2 state before reaching the AFM state. At low temperatures, the AFM state of the Mn sublattice will change to the canted-AFM-2 state through the field-induced metamagnetic transition. The Nd sublattice displays an AFM order below $T_{N4\perp}$ when H is less than 23.1 kOe. When H is larger than 23.1 kOe, a field-induced FM state is reached for Nd sublattice. Though magnetic phase diagrams for $H\|c$ and $H \perp c$ are a little different, AFM ground states are proposed for both $H\|c$ and $H \perp c$ cases because the $M(H)$ curves of NdMn$_{0.88}$Sb$_2$ measured at 2 K show linear

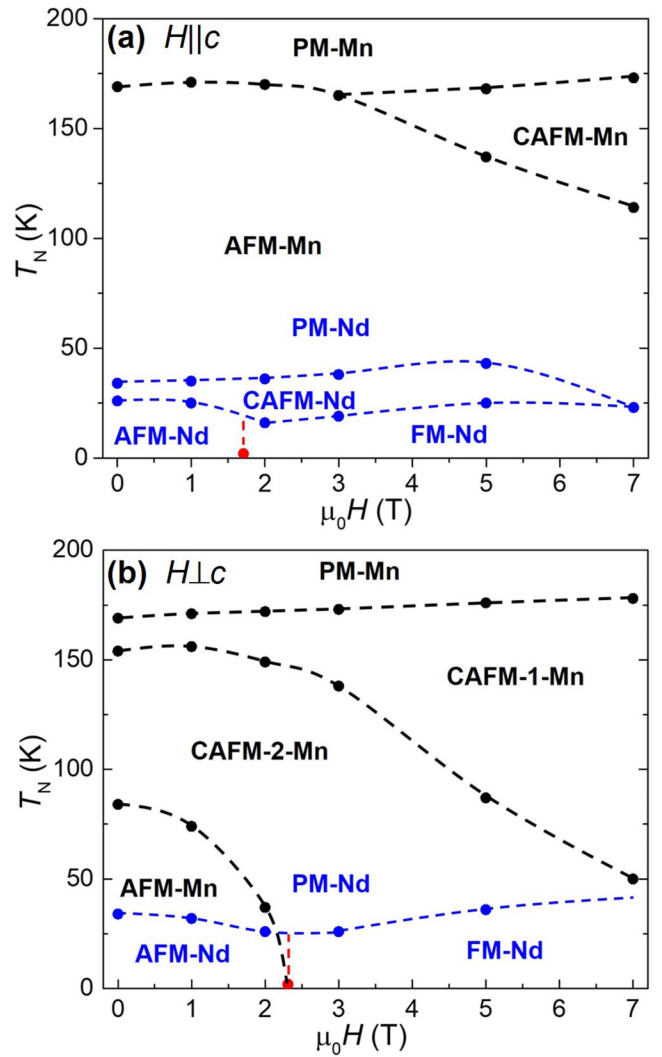FIG. 6. (a) Magnetic phase diagram of NdMn$_{0.88}$Sb$_2$ with $H\|c$; (b) Magnetic phase diagram of NdMn$_{0.88}$Sb$_2$ with $H \perp c$. The red dots and red dashed lines indicate the critical fields for the spin flop transitions and the estimated boundary between AFM and FM state for Nd sublattice, respectively. PM = paramagnetic; CAFM = canted-AFM.

behavior before the spin-flop transition for both $H\|c$ and $H \perp c$ cases. Field-induced spin-flop transitions for Nd sublattice are observed for both $H\|c$ and $H \perp c$ cases with $H_{SF\|} = 17.1$ kOe and $H_{SF\perp} = 23.1$ kOe, respectively, at 2 K. There is no strong magnetic anisotropy for NdMn$_{0.88}$Sb$_2$. The transitions above the AFM-Mn and AFM-Nd are defined as canted-AFM-Mn and canted-AFM-Nd transitions in these magnetic phase diagrams to be consistent with their AFM ground state. However, these canted-AFM transitions may also be regarded as weak-FM transitions. Studies of polycrystalline NdMnSb$_2$ reported a weak-FM transition at ~ 250 K for the Mn sublattice [17]. In this work, the magnetic order temperature for Mn sublattice (~ 170 K) is lower than that reported for the polycrystalline sample, and the magnetic order at ~ 34 K for Nd sublattice is a little lower than that reported in the polycrystalline NdMnSb$_2$ (45 K) [17].
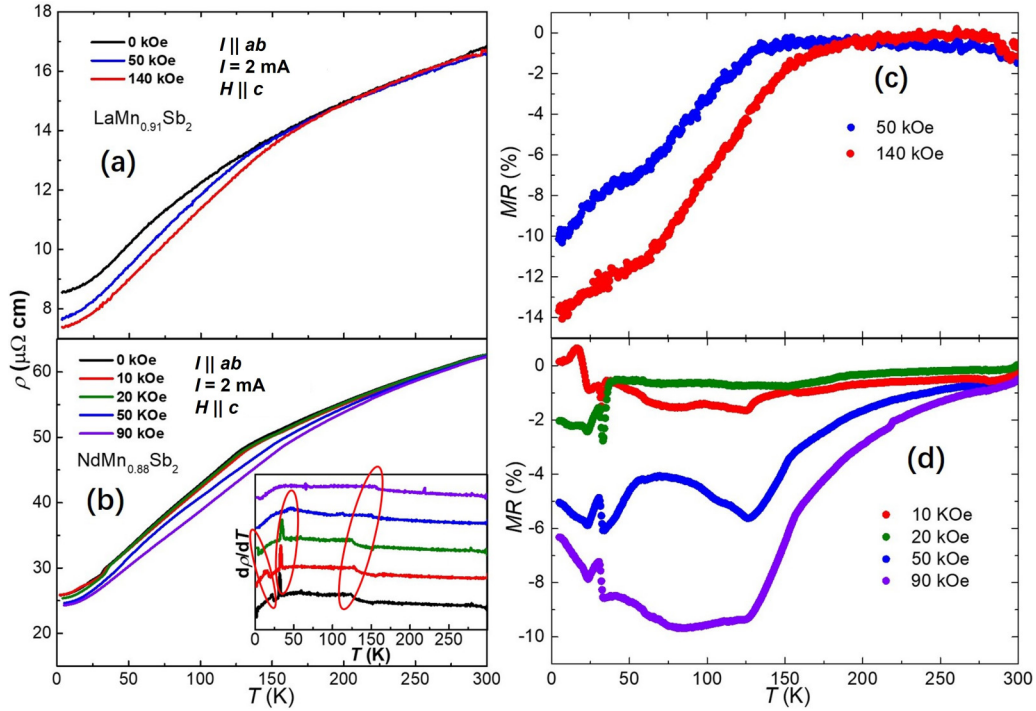
FIG. 7. (a) and (b) Temperature-dependent resistivity measured under varied H for LaMn$_{0.91}$Sb$_2$ and NdMn$_{0.88}$Sb$_2$, respectively. Inset in (b) shows the corresponding dρ/dT curve for NdMn$_{0.88}$Sb$_2$, and red elliptical curves are just for eyes. (c) and (d) Temperature-dependent magnetoresistance under varied H for LaMn$_{0.91}$Sb$_2$ and NdMn$_{0.88}$Sb$_2$, respectively.

Temperature-dependent of resistivity, $\rho(T)$, for LaMn$_{0.91}$Sb$_2$ and NdMn$_{0.88}$Sb$_2$ are shown in Figs. 7(a) and 7(b), respectively. On cooling, a metallic behavior was observed for both LaMn$_{0.91}$Sb$_2$ and NdMn$_{0.88}$Sb$_2$. The residual resistivity ratio defined as $\rho(300K)/\rho(2K)$ is ~ 2.0 for LaMn$_{0.91}$Sb$_2$ and ~ 2.5 for NdMn$_{0.88}$Sb$_2$, indicating bad metals. For the $\rho(T)$ curve of LaMn$_{0.91}$Sb$_2$ measured without a magnetic field, there is no kink or anomaly observed corresponding to the magnetic orders of Mn sublattice ($\sim$130 K). When measured under an H of 50 kOe, negative magnetoresistance (MR) emerges below $\sim$130K [see Fig. 7(c)], which is possibly related to the field-induced weak FM state of the Mn sublattice. The negative MR is further enhanced when measured under 140 kOe, and the maximum MR is about -13.7% at 2 K and under 140 kOe [see Fig. 7(c)]. The MR was calculated by equation MR $= 100\% \times [\rho(H) - \rho(0)]/\rho(0)$, where $\rho(H)$ and $\rho(0)$ are ρ measured under H and without H, respectively. The $\rho(T)$ curve of NdMn$_{0.88}$Sb$_2$ measured without magnetic field shows kinks at $\sim$125, $\sim$32, and $\sim$23 K. The drop of ρ at $\sim$125 K is possibly attributed to the AFM order of Mn sublattice, though this temperature is little lower than the $T_{N1||}$ of 170 K. The drop of ρ at $\sim$32 and $\sim$23 K is possibly related to the magnetic orders of Nd sublattice at $T_{N2||}$ of 34 K and $T_{N3||}$ of 26 K, respectively. The magnetic orders would generally reduce the scattering of conduction electrons by paramagnetic fluctuations, responsible for the drop of ρ. From the corresponding dρ/dT curve [see the inset in Fig. 7(b)], kinks around $\sim$125 K are robust up to 30 kOe and shift to $\sim$150 K when H is 50 and 70 kOe. With the increase of H, anomalies around 32 and 23 K shift toward higher and lower temperatures, respectively, which is consistent with the shift of $T_{N2||}$ and $T_{N3||}$ under varied H, further confirming their relevance. Compared with the curve measured without H, $\rho(T)$ curves of NdMn$_{0.88}$Sb$_2$ measured under 10 and 20 kOe ($H||c$) do not show clear MR. MR can be observed below 250 K for the $\rho(T)$ curves measured with 50 and 90 kOe. The MR increases with cooling and reaches maximums around $\sim$ 125 K, indicating the long-range AFM order of Mn sublattice goes against the negative MR. Recalling the magnetic phase diagram for NdMn$_{0.88}$Sb$_2$ with $H||c$, the Mn sublattice first undergoes a canted-AFM state before reaching the AFM state when H is larger than 30 kOe. It seems that the canted AFM state of Mn sublattice in NdMn$_{0.88}$Sb$_2$ is related to the negative MR, which is also indicated by the $\rho(T)$ data of LaMn$_{0.91}$Sb$_2$. Magnetic orders of Nd sublattice do not have a significant contribution to the negative MR.

IV. CONCLUSION

Single crystals of LaMn$_{0.91}$Sb$_2$ and NdMn$_{0.88}$Sb$_2$ have been successively grown by using the Bi-flux method. They all crystallize in the HfCuSi$_2$-type tetragonal structure with space group *P4/nmm* (No.129). Analysis of the single-crystal x-ray diffraction data suggests moderate deficiencies of Mn in both compounds and the refined compositions are LaMn$_{0.91}$Sb$_2$ and NdMn$_{0.88}$Sb$_2$. Signs of successive AFM transitions are observed at 133 and 108 K for LaMn$_{0.91}$Sb$_2$ with $H||c$. In the case of $H \perp c$, the LaMn$_{0.91}$Sb$_2$ shows a weak FM transition around 138 K and an AFM transition at 56 K. However, there is no anomaly observed in the $C_p(T)$ curve. Magnetic phase diagrams for NdMn$_{0.88}$Sb$_2$ are

depicted according to its $M(T)$, $M(H)$, and $C_p(T)$ data. When $H||c$ and H is no more than 30 kOe, the Mn sublattice goes into an AFM order below $T_{N1||}$. When H is larger than 30 kOe, the Mn sublattice first undergoes a canted-AFM state before reaching the AFM state. The Nd sublattice first undergoes a canted-AFM state below $T_{N2||}$ before reaching the AFM state. The AFM state of Nd sublattice can be induced to be an FM state by H through a spin-flop transition with $H_{SF||} = 17.1$ kOe at 2 K. For $H\perp c$, the Mn sublattice undergoes a canted-AFM-1 state and a canted-AFM-2 state before reaching the AFM state. The Nd sublattice displays an AFM order below $T_{N4\perp}$ when H is less than 23.1 kOe. The FM state for the Nd sublattice is induced by H at 2 K when H is larger than $H_{SF\perp}$ of 23.1 kOe. Analysis of the $\rho(T)$ curves of $LaMn_{0.91}Sb_2$ and $NdMn_{0.88}Sb_2$ measured with varied H indicates that $LaMn_{0.91}Sb_2$ and $NdMn_{0.88}Sb_2$ all show metallic behavior and the negative MR in $LaMn_{0.91}Sb_2$ and

$NdMn_{0.88}Sb_2$ are possibly related with the canted-AFM orders of Mn sublattice.

[1] J. Y. Liu, J. Hu, Q. Zhang, D. Graf, H. B. Cao, S. M. A. Radmanesh, D. J. Adams, Y. L. Zhu, G. F. Cheng, X. Liu, W. A. Phelan, J. Wei, M. Jaime, F. Balakirev, D. A. Tennant, J. F. DiTusa, I. Chiorescu, L. Spinu, and Z. Q. Mao, A magnetic topological semimetal $Sr_{1-y}Mn_{1-z}Sb_2$ (y, z < 0.1), Nat. Mater. **16**, 905 (2017).

[2] M. A. Farhan, G. Lee, and J. H. Shim, AEMnSb$_2$ (AE = Sr, Ba): A new class of Dirac materials, J. Phys.: Condens. Matter **26**, 042201 (2014).

[3] G. Lee, M. A. Farhan, J. S. Kim, and J. H. Shim, Anisotropic Dirac electronic structures of AMnBi$_2$ (A = Sr, Ca), Phys. Rev. B **87**, 245104 (2013).

[4] A. F. May, M. A. McGuire, and B. C. Sales, Effect of Eu magnetism on the electronic properties of the candidate Dirac material EuMnBi$_2$, Phys. Rev. B **90**, 075109 (2014).

[5] M. M. Piva, R. Tartaglia, G. S. Freitas, J. C. Souza, D. S. Christovam, S. M. Thomas, J. B. Leão, W. Ratcliff, J. W. Lynn, C. Lane, J.-X. Zhu, J. D. Thompson, P. F. S. Rosa, C. Adriano, E. Granado, and P. G. Pagliuso, Electronic and magnetic properties of stoichiometric CeAuBi$_2$, Phys. Rev. B **101**, 214431 (2020).

[6] C. B. R. Jesus, M. M. Piva, P. F. S. Rosa, C. Adriano, and P. G. Pagliuso, Evolution of the magnetic properties along the RCuBi$_2$ (R = Ce, Pr, Nd, Gd, Sm) series of intermetallic compounds, J. Appl. Phys. **115**, 17E115 (2014).

[7] P. F. S. Rosa, Y. Luo, E. D. Bauer, J. D. Thompson, P. G. Pagliuso, and Z. Fisk, Ferromagnetic Kondo behavior in UAuBi$_2$ single crystals, Phys. Rev. B **92**, 104425 (2015).

[8] J. B. He, D. M. Wang, and G. F. Chen, Giant magnetoresistance in layered manganese pnictide CaMnBi$_2$, Appl. Phys. Lett. **100**, 112405 (2012).

[9] S. K. Malik, Z. Chu, A. G. Joshi, J. B. Yang, W. B. Yelon, Q. Cai, W. J. James, and K. Kamaraju, Magnetic and neutron diffraction studies on PrMnSb$_2$, J. Appl. Phys. **91**, 7842 (2002).

[10] L. Balicas, S. Nakatsuji, H. Lee, P. Schlottmann, T. P. Murphy, and Z. Fisk, Magnetic field-tuned quantum critical point in CeAuSb$_2$, Phys. Rev. B **72**, 064422 (2005).

[11] A. Wang, S. Baranets, Y. Liu, X. Tong, E. Stavitski, J. Zhang, Y. Chai, W.-G. Yin, S. Bobev, and C. Petrovic, Magnetic mixed

valent semimetal EuZnSb$_2$ with Dirac states in the band structure, Phys. Rev. Research **2**, 033462 (2020).

[12] C. Adriano, P. F. S. Rosa, C. B. R. Jesus, T. Grant, Z. Fisk, D. J. Garcia, and P. G. Pagliuso, Magnetic properties of nearly stoichiometric CeAuBi$_2$ heavy fermion compound, J. Appl. Phys. **117**, 17C103 (2015).

[13] J. Liu, P. Liu, K. Gordon, E. Emmanouilidou, J. Xing, D. Graf, B. C. Chakoumakos, Y. Wu, H. Cao, D. Dessau, Q. Liu, and N. Ni, Nontrivial topology in the layered Dirac nodal-line semimetal candidate SrZnSb$_2$ with distorted Sb square nets, Phys. Rev. B **100**, 195123 (2019).

[14] E. M. Seibel, W. Xie, Q. D. Gibson, and R. J. Cava, Structure and magnetic properties of the REAuBi$_2$ (RE = La–Nd, Sm) phases, J. Solid State Chem. **230**, 318 (2015).

[15] O. Ya. Zelinska and A. Mar, Structure and physical properties of rare-earth zinc antimonides REZn$_{1-X}$Sb$_2$ (RE = La, Ce, Pr, Nd, Sm, Gd, Tb), J. Solid State Chem. **179**, 3776 (2006).

[16] P. Wollesen, W. Jeitschko, M. Brylak, and L. Dietrich, Ternary antimonides LnM$_{1-x}$Sb$_2$ with ln = La, Nd, Sm, Gd, Tb and M = Mn, Co, Au, Zn, Cd, J. Alloys Compd. **245**, L5 (1996).

[17] O. Sologub, K. Hiebl, P. Rogl, and O. Bodak, Ternary compounds REMSb$_2$, RE = La, Ce, Pr, Nd, Sm, Gd; M = Mn, Zn, Cd; Compound Formation, crystal structure and magnetism, J. Alloys Compd. **227**, 40 (1995).

[18] J. B. He, Y. Fu, L. X. Zhao, H. Liang, D. Chen, Y. M. Leng, X. M. Wang, J. Li, S. Zhang, M. Q. Xue, C. H. Li, P. Zhang, Z. A. Ren, and G. F. Chen, Quasi-Two-Dimensional massless Dirac fermions in CaMnSb$_2$, Phys. Rev. B **95**, 045128 (2017).

[19] S. Klemenz, S. M. Lei, and L. M. Schoop, Topological semimetals in square-net materials, Annu Rev. Mater. Res. **49**, 185 (2019).

[20] J. Y. Liu, J. Yu, J. L. Ning, H. M. Yi, L. Miao, L. J. Min, Y. F. Zhao, W. Ning, K. A. Lopez, Y. L. Zhu, T. Pillsbury, Y. B. Zhang, Y. Wang, J. Hu, H. B. Cao, F. Balakirev, F. Weickert, M. Jaime, Y. Lai, K. Yang, J. W. Sun, N. Alem, V. Gopalan, C. Z. Chang, N. Samarth, C. X. Liu, R. D. Mcdonald, and Z. Q. Mao, Spin-Valley Locking, bulk quantum Hall effect and chiral surface state in a noncentrosymmetric Dirac semimetal BaMnSb$_2$, Nat. Commun. **12**, 4062 (2021).

[21] H. Masuda, H. Sakai, M. Tokunaga, Y. Yamasaki, A. Miyake, J. Shiogai, S. Nakamura, S. Awaji, A. Tsukazaki, H. Nakao, Y. Murakami, T. Arima, Y. Tokura, and S. Ishiwata, Quantum Hall effect in a bulk antiferromagnet EuMnBi$_2$ with magnetically confined two-dimensional Dirac fermions, Sci. Adv. **2**, e1501117 (2016).

[22] C. Yi, S. Yang, M. Yang, L. Wang, Y. Matsushita, S. Miao, Y. Jiao, J. Cheng, Y. Li, K. Yamaura, Y. Shi, and J. Luo, Large negative magnetoresistance of a nearly Dirac material: layered antimonide EuMnSb$_2$, Phys. Rev. B **96**, 205103 (2017).

[23] Z. L. Sun, A. F. Wang, H. M. Mu, H. H. Wang, Z. F. Wang, T. Wu, Z. Y. Wang, X. Y. Zhou, and X. H. Chen, Field-Induced Metal-to-Insulator transition and colossal anisotropic magnetoresistance in a nearly Dirac material EuMnSb$_2$, npj Quantum Mater. **6**, 94 (2021).

[24] S. Baranets and S. Bobev, Transport properties and thermal behavior of YbMnSb$_2$ semimetal above room temperature, J. Solid State Chem. **303**, 122467 (2021).

[25] J. Y. Liu, J. Hu, D. Graf, T. Zou, M. Zhu, Y. Shi, S. Che, S. M. A. Radmanesh, C. N. Lau, L. Spinu, H. B. Cao, X. Ke, and Z. Q. Mao, Unusual interlayer quantum transport behavior caused by the zeroth landau level in YbMnBi$_2$, Nat. Commun. **8**, 646 (2017).

[26] Y.-Y. Wang, S. Xu, L.-L. Sun, and T.-L. Xia, Quantum oscillations and coherent interlayer transport in a new topological Dirac semimetal candidate YbMnSb$_2$, Phys. Rev. Materials **2**, 021201(R) (2018).

[27] J.-R. Soh, S. M. Tobin, H. Su, I. Zivkovic, B. Ouladdiaf, A. Stunault, J. A. Rodríguez-Velamazán, K. Beauvois, Y. Guo, and A. T. Boothroyd, Magnetic structure of the topological semimetal YbMnSb$_2$, Phys. Rev. B **104**, L161103 (2021).

[28] Y. Takahashi, T. Urata, and H. Ikuta, Metamagnetic transitions associated with two antiferromagnetic phases of PrMn$_{1-x}$Sb$_2$ and its magnetic phase diagram, Phys. Rev. B **104**, 054408 (2021).

[29] J.-R. Soh, P. Manuel, N. M. B. Schröter, C. J. Yi, D. Prabhakaran, F. Orlandi, Y. G. Shi, and A. T. Boothroyd, Magnetic and electronic structure of Dirac semimetal candidate EuMnSb$_2$, Phys. Rev. B **100**, 174406 (2019).

[30] APEX3 Ver. 2015, Bruker AXS, Inc., Madison, WI (2015).

[31] G. M. Sheldrick and T. R. Schneider, SHELXL: High-resolution refinement, Methods Enzymol. **277**, 319 (1997).

[32] G. M. Sheldrick, A short history of SHELX, Acta Crystal. Sec. A **64**, 112 (2008).

[33] B. H. Toby and R. B. Von Dreele, GSAS-II: the genesis of a modern open-source all purpose crystallography software package, J. Appl. Cryst. **46**, 544 (2013).

[34] See Supplemental Material at http://link.aps.org/supplemental/10.1103/PhysRevB.105.224429 for details on Crystallographic data for NdMn$_{0.88}$Sb$_2$ and LaMn$_{0.91}$Sb$_2$; Refined atomic coordinates and equivalent isotropic thermal parameters for LaMn$_{0.91}$Sb$_2$ and NdMn$_{0.88}$Sb$_2$; Detailed analysis of $M(T)$ and $M(H)$ curves for LaMn$_{0.91}$Sb$_2$ and NdMn$_{0.88}$Sb$_2$; Crystallographic information files (Cif) for LaMn$_{0.91}$Sb$_2$ and NdMn$_{0.88}$Sb$_2$.

[35] G. Markandeyulu and K. V. S. Rama Rao, Spin reorientation in MnSb single crystals by FMR, J. Magn. Magn. Mater. **67**, 215 (1987).

[36] A. Wang, I. Zaliznyak, W. Ren, L. Wu, D. Graf, V. O. Garlea, J. B. Warren, E. Bozin, Y. Zhu, and C. Petrovic, Magnetotransport study of Dirac fermions in YbMnBi$_2$ antiferromagnet, Phys. Rev. B **94**, 165161 (2016).

[37] J.-R. Soh, H. Jacobsen, B. Ouladdiaf, A. Ivanov, A. Piovano, T. Tejsner, Z. Feng, H. Wang, H. Su, Y. Guo, Y. Shi, and A. T. Boothroyd, Magnetic structure and excitations of the topological semimetal YbMnBi$_2$, Phys. Rev. B **100**, 144431 (2019).

[38] D. Gong, S. Huang, F. Ye, X. Gui, J. Zhang, W. Xie, and R. Y. Jin, Canted Eu magnetic structure in EuMnSb$_2$, Phys. Rev. B **101**, 224422 (2020).

[39] A. Paduan-Filho, C. C. Becerra, and F. Palacio, Hysteresis at the spin-flop transition in the antiferromagnets K$_2$Fe (Cl$_{1-x}$Br$_x$)$_5 \bullet$ H$_2$O, Phys. Rev. B **43**, 11107 (1991).

[40] G. André, F. Bourée, A. Oleś, B. Penc, W. Sikora, A. Szytula, and A. Zygmunt, Magnetic ordering of RNiSb$_2$ (R = Pr, Nd and Tb) compounds studied by neutron diffraction and magnetic measurements,, J. Alloys Compd. **255**, 31 (1997).